

















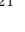



ALMA-QUARKS: Few-Thousand-Year Hatching out of “Egg”: The Supersonic Breakout of a Hypercompact H II Region from Its Parental Hot Core

SIJU ZHANG ^{1,2} GUIDO GARAY ^{1,2} FENGWEI XU ^{3,4} LUIS F. RODRÍGUEZ ⁵ NEAL J. EVANS II ⁶
ANNIE ZAVAGNO ^{7,8} PAUL F. GOLDSMITH ⁹ DONGTING YANG ¹⁰ XUNCHUAN LIU ¹¹ AIYUAN YANG ^{12,13}
TIE LIU ¹¹ AMELIA M. STUTZ ¹⁴ HONG-LI LIU ¹⁰ WENYU JIAO ¹¹ ANANDMAYEE TEJ ¹⁵ LEI ZHU,²
KEE-TAE KIM ^{16,17} PABLO GARCÍA ¹⁸ THOMAS PETERS,¹⁹ THOMAS MÖLLER ²⁰ SHANGHUO LI ²¹ AND
LEONARDO BRONFMAN ¹

¹Departamento de Astronomía, Universidad de Chile, Camino el Observatorio 1515, Las Condes, Santiago, Chile

²Chinese Academy of Sciences South America Center for Astronomy, National Astronomical Observatories, CAS, Beijing 100101, China

³Kavli Institute for Astronomy and Astrophysics, Peking University, 5 Yiheyuan Road, Haidian District, Beijing 100871, China

⁴Max Planck Institute for Astronomy, Königstuhl 17, 69117 Heidelberg, Germany

⁵Instituto de Radioastronomía y Astrofísica, Universidad Nacional Autónoma de México, Apdo. Postal 3-72, Morelia, Michoacán 58089, Mexico

⁶Department of Astronomy, The University of Texas at Austin, 2515 Speedway, Austin, TX 78712, USA

⁷Aix Marseille Univ, CNRS, CNES, LAM, F-13388 Marseille, France

⁸Institut Universitaire de France, Paris, 1 rue Descartes, F-75231 Paris Cedex 05, France

⁹Jet Propulsion Laboratory, California Institute of Technology, 4800 Oak Grove Drive, Pasadena CA 91109, USA

¹⁰School of Physics and Astronomy, Yunnan University, Kunming, 650091, China

¹¹Shanghai Astronomical Observatory, Chinese Academy of Sciences, Shanghai 200030, China

¹²National Astronomical Observatories, Chinese Academy of Sciences, Beijing 100101, China

¹³Key Laboratory of Radio Astronomy and Technology, Chinese Academy of Sciences, A20 Datun Road, Chaoyang District, Beijing, 100101, China

¹⁴Departamento de Astronomía, Universidad de Concepción, Casilla 160-C, Concepción, Chile

¹⁵Indian Institute of Space Science and Technology, Thiruvananthapuram 695 547, Kerala, India

¹⁶Korea Astronomy and Space Science Institute, 776 Daedeokdae-ro, Yuseong-gu, Daejeon 34055, Republic of Korea

¹⁷University of Science and Technology, Korea (UST), 217 Gajeong-ro, Yuseong-gu, Daejeon 34113, Republic of Korea

¹⁸Instituto de Astronomía, Universidad Católica del Norte, Av. Angamos 0610, Antofagasta, Chile

¹⁹Max-Planck-Institut für Astrophysik, Karl-Schwarzschild-Str. 1, D-85748 Garching, Germany

²⁰I. Physikalisches Institut der Universität zu Köln, Zùlpicher Str. 77, 50937, Köln, Germany

²¹School of Astronomy and Space Science, Nanjing University, Nanjing 210093

ABSTRACT

The kinematic evolution of hypercompact H II (HC H II) regions around young high-mass stars remains poorly understood due to complex interactions with parental environs. We present ALMA QUARKS/ATOMS 1.3 mm/3 mm observations (the highest resolution ~ 0.01 pc) of a deeply embedded HC H II region (diameter ~ 0.015 pc, electron density $\sim 2 \times 10^5$ cm⁻³) exhibiting a striking $\gtrsim 20$ km s⁻¹ global redshift seen in optically thin H30 α /H40 α recombination lines relative to its parental hot molecular core within a hub-filament system. The 1.3 mm continuum data reveal a distinct 0.1-pc arc and a perpendicular 0.04-pc tail. We propose that this morphology arises from a dynamic champagne flow: the slow expansion of HC H II region into a pre-existing filament forms the arc and associated low-velocity (few km s⁻¹) SiO shocks. Meanwhile, in the opposite direction ionized gas escapes along a steep density gradient traced by the tail and high-velocity (20 km s⁻¹) SiO emission. We reject the bow shock scenario in which ionized gas co-moves with a runaway high-mass star because shocked gas in the arc aligns with the hub velocity, contradicting the bow shock prediction. Non-LTE radiative transfer modeling further rules out infall of ionized gas as the velocity shift origin. We conclude that this exceptional HC H II region is undergoing a few-thousand-year transition phase of

“hatching out of the egg”: the ionized gas of HC H II region has just broken out of its parental hot core and now is flowing outward supersonically. This work highlights how anisotropic density distributions induce supersonically anisotropic ionized flows that govern HC H II region evolution.

Keywords: Star formation(1569) — H II regions(694) — Molecular clouds(7) — Supersonic expansion(2242)

1. INTRODUCTION

The formation of high-mass stars is markedly more complex than that of low-mass stars, owing to intense feedback such as photoionization and stellar winds (Beuther et al. 2025; Suin et al. 2025). The ultraviolet radiation emitted by nascent high-mass stars ionizes the surrounding neutral medium, generating hypercompact H II (HC H II) regions (electron density $n_e \gtrsim 10^6 \text{ cm}^{-3}$ and diameter $D \lesssim 0.03 \text{ pc}$) that suppress sustained accretion and evolve through phases of expansion, eventually transitioning to classical H II regions (Kurtz 2005). Investigating the kinematics of these nascent HC H II regions is therefore critical to elucidate the early stages of high-mass star formation (HMSF). Observations and numerical simulations have revealed intricate gas kinematic processes in HC H II regions, including molecular/ionized disk-jet systems (Guzmán et al. 2020; Moscadelli et al. 2021; Miyawaki et al. 2023), accretion/infall in ionized and molecular flows (Keto 2003; Peters et al. 2010a,b; Komesch et al. 2024), and highly variable expansion or even contraction (Galván-Madrid et al. 2008; Peters et al. 2010a; De Pree et al. 2014; Yang et al. 2025a).

The kinematics of H II regions is intrinsically linked to their parental molecular clumps, often inheriting their systemic velocities from the precursor clumps (Li et al. 2023). However, this inheritance correlation breaks down if the ionizing sources are runaway stars originating externally or if the ionized gas breaks out and escapes from the natal clump. Depending on stellar motion within the natal clump, ionized gas may co-move with the ionizing star to form bow shocks (van Buren et al. 1990) or flow along density gradients as champagne flows (Tenorio-Tagle 1979). Previous observations of such dynamical systems frequently focused on ultracompact H II (UC H II) regions ($n_e \gtrsim 10^4 \text{ cm}^{-3}$ and $D \lesssim 0.1 \text{ pc}$) that exhibit cometary morphologies (Garay & Lizano 1999; Kim & Koo 2001, 2003; Churchwell 2002; Hoare 2005; Hoare et al. 2007; Zhang et al. 2024, and references therein), due to the scarcity and compactness of HC H II regions (Yang et al. 2019, 2021). Furthermore, high-frequency radio recombination lines (RRLs) at mm wavelength are essential to characterize the kinematics of ionized gas at extremely high density because

they suffer less from pressure broadening, non-LTE effects, and ensure optically thin conditions (Keto 2003; Peters et al. 2012).

To trace the dynamical decoupling between the ionized gas and the parental molecular clump, we analyzed the offsets of systemic velocity measured with mm RRLs and molecular lines in two surveys, shown in Fig. 1. Panel (a) shows the parsec-scale velocity offsets in single-dish surveys of ATLASGAL clumps (Kim et al. 2017) and panel (b) shows the ATOMS (ALMA Three-millimeter Observations of Massive Star-forming regions, resolution $\sim 1.5''$; Liu et al. 2020, 2021) observations of UC and HC H II regions still embedded in molecular clumps. Line tracers are the same within each survey. From Figure 1, we can see that extreme velocity shifts ($> 20 \text{ km s}^{-1}$) are very rare ($< 2\%$) among the detected clumps and cores. In particular, the HC H II region in IRAS 19095+0930 (I19095 hereafter; Liu et al. 2021) exhibits the most extreme velocity shift and compactness within the sample. The other two H II regions with an extreme velocity shift ($> 20 \text{ km s}^{-1}$) are found to have explosive outflows (Zapata et al. 2023) or locate in the Central Molecular Zone (thus hard to determine clump velocity).

Here, we present I19095 ATOMS and high-resolution ($\sim 0.3''$) ALMA-QUARKS observations (Querying Underlying mechanisms of massive star formation with ALMA-Resolved gas Kinematics and Structures; Liu et al. 2024). Our analysis reveals that the kinematics of this HC H II region can be interpreted as a champagne flow associated with a hot core and defies interpretation in terms of bow shocks or infalling ionized gas under non-LTE conditions. Our observations of this source challenge the assumption of spherically symmetric expansion even for the earliest H II regions and invoke a very rapid transition phase of “hatching out of the egg” in the hot core-HC H II region evolution.

2. ALMA DATA

QUARKS 1.3 mm data combine observations from the 12 m main array (configurations C-2 and C-5) and the Atacama Compact Array (ACA) 7 m array to achieve an angular resolution of $0.35''$ and maximum recoverable scale (MRS) of $\sim 30''$. The continuum sensitivity

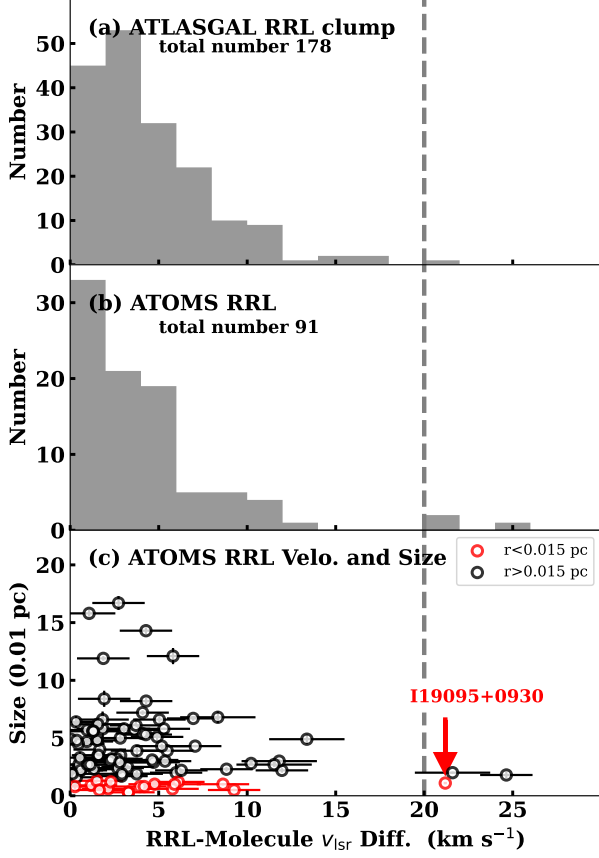


Figure 1. Velocity shifts between mm RRLs and molecular lines in high-mass star-forming molecular clumps. Vertical dashed line highlights the shift of 20 km s^{-1} . (a) Single-dish survey of 976 ATLASGAL clumps (RRLs detected in 178 sources; Kim et al. 2017). (b) Velocity shifts for 91 embedded HC and UC H II regions, identified across 146 ATOMS molecular clumps (Liu et al. 2021). (c) Size (radius)-velocity shift relation for 91 ATOMS HC or UC H II regions, highlighting compactness and extreme kinematics of I19095.

reaches $\sim 0.12 \text{ mJy beam}^{-1}$, with spectral line data binned at a channel width of 0.63 km s^{-1} and a sensitivity of $\sim 0.4 \text{ K}$. More details on the QUARKS dataset are provided in Liu et al. (2024); Xu et al. (2024); Yang et al. (2025b).

ATOMS 3 mm data combine the observations in the C-3 configuration and the ACA 7m array. The 12 m and 7 m data sets were subsequently combined and imaged jointly using CASA 6.6.0 (CASA Team et al. 2022). The final continuum image achieves a sensitivity of $0.13 \text{ mJy beam}^{-1}$, with phase solutions derived from the continuum applied to the spectral cubes. The angular resolution and MRS are $1.58''$ and $\sim 60''$, respectively, with spectral channels of 1.48 km s^{-1} width and a sensitivity of 0.11 K for $\text{H}40\alpha$ and 0.21 km s^{-1} and 0.3 K for $\text{H}^{13}\text{CO}^+ J = 1 - 0$ (Liu et al. 2020).

To improve image fidelity and dynamic range, three rounds of phase self-calibration were applied to both the QUARKS and ATOMS data, effectively reducing side-lobes caused by phase errors.

3. PARENTAL HUB-FILAMENT SYSTEM

The region I19095, also known as the hydroxyl maser source OH 43.8–0.1 (Winnberg et al. 1975), is a highly active site of HMSF, evidenced by the detection of numerous molecular masers. These include OH masers at 1.66 GHz (Fish et al. 2005) and 6.03 GHz (Baudry et al. 1997), H_2O masers at 22 GHz (Honma et al. 2005), and CH_3OH Class I (44 GHz ; Kim et al. 2019) and Class II (6.7 GHz ; Surcis et al. 2019) masers. Most of the masers are concentrated near the systemic velocity of the local standard of rest $v_{\text{LSR}} \sim 43 \text{ km s}^{-1}$, spanning a range of a few km s^{-1} . Trigonometric parallax measurements of H_2O masers yield a distance of $6.02^{+0.39}_{-0.34} \text{ kpc}$ (Wu et al. 2019). At this distance, the natal clump traced by the ATLASGAL $870 \mu\text{m}$ emission has a mass of $\sim 530 M_{\odot}$, a radius of 0.24 pc , with a dust temperature T_{dust} of 35 K (Urquhart et al. 2022).

3.1. Velocity-coherent hub-filament system

Figure 2a displays the 0th moment map integrated from $v_{\text{LSR}} = 35$ to 55 km s^{-1} of ATOMS $\text{H}^{13}\text{CO}^+ J = 1 - 0$ emission that well traces the dense gas in the HMSF regions (Zhang et al. 2024). At least five filamentary structures (F1–F5), identified using the FilFinder algorithm (Koch & Rosolowsky 2015), converge to the central hub. The filament skeletons, color-coded by v_{LSR} of H^{13}CO^+ , reveal that the entire hub-filament system (HFS) is velocity-coherent, centered at $v_{\text{LSR}} \simeq 43 \text{ km s}^{-1}$. Notably, some filaments (e.g., F3 and F4) exhibit significant velocity gradients toward the hub, while others show non-monotonic gradients, suggesting complex 3D projection effects if sustained inflow occurs. The filament with the most prominent velocity gradient, F4, shows a projected velocity gradient of $\gtrsim 1 \text{ km s}^{-1} \text{ pc}^{-1}$. Assuming an H_2 column density of $\sim 10^{23} \text{ cm}^{-2}$ derived from H^{13}CO^+ using the methods in Zhang et al. (2024), this gradient implies an inflow rate of $\sim 0.1 M_{\odot} \text{ kyr}^{-1}$. The total ongoing mass accretion into the hub, if all converging filaments are counted, is therefore likely on the order of $0.1 M_{\odot} \text{ kyr}^{-1}$.

3.2. 3-mm cores and spatially correlated $\text{H}40\alpha$

The ATOMS 3 mm continuum image (Fig. 2b) reveals two compact sources associated with the ATOMS $\text{H}40\alpha$ line emission which are shown in Fig. 3: *Main Core* (located within the hub) and *East Core* (offsets from the hub). Both cores are associated with known H II

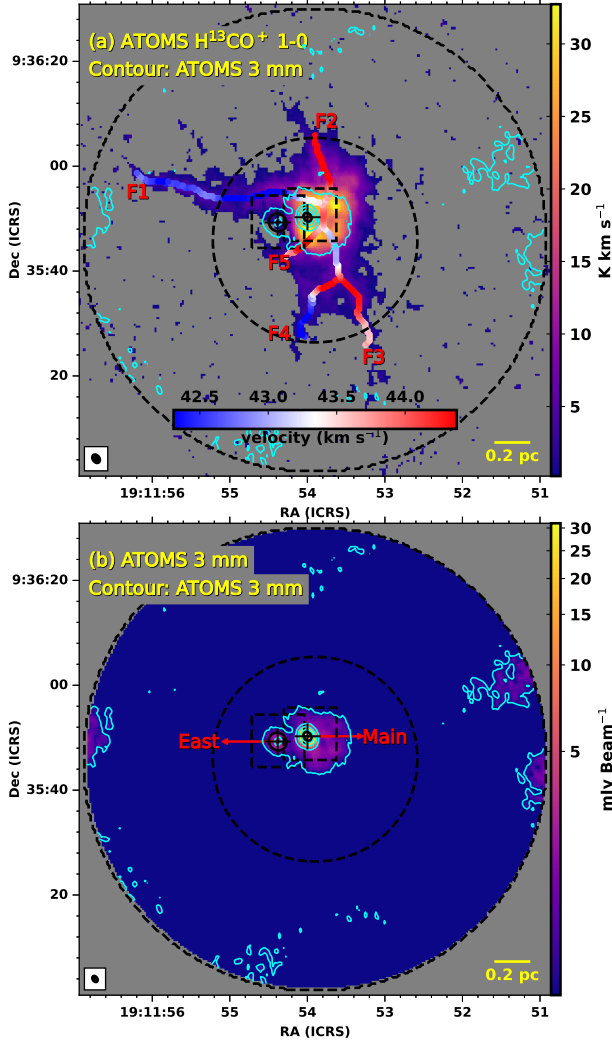


Figure 2. ATOMS view of the I19095 hub-filament system and the two embedded 3 mm cores. (a) ATOMS $\text{H}^{13}\text{CO}^+ J=1-0$ 0th moment map (3 σ channel threshold), overlaid with ATOMS 3 mm contours (levels: 0.72–222 mJy beam $^{-1}$ in 5 logarithmic steps) and filament skeletons (F1–F5) color-coded by their v_{lsr} . (b) ATOMS 3 mm continuum emission, with ellipses denoting Gaussian FWHM sizes for the cores, crosses making the core centers, boxes indicating zoom-in regions shown in Fig. 3, and circles marking the fields of view of ATOMS and QUARKS.

regions detected in earlier VLA centimeter-wavelength observations (Kurtz et al. 1994; Kalcheva et al. 2018) and the two cores have a separation of $\sim 5.7''$ (equivalent to 0.17 pc). The Main Core remains unresolved in the ATOMS continuum image. A Gaussian fit using CASA `imfit` fails to yield a deconvolved size and returns only a beam-convolved FWHM $1.8'' \times 1.4''$ (0.05 pc \times 0.04 pc) with a flux density of 224 ± 7.6 mJy. The East Core, previously undetected in the ATOMS survey, is clearly

detected in the present study due to the improved data reduction (Liu et al. 2021).

The strong $\text{H}40\alpha$ suggests that free-free emission dominates the 3 mm continuum emission of the Main Core. The simplified expression for the free-free continuum-to-RRL ratio derived by Garay et al. (1986), under the assumption of optically thin continuum emission (Sect. 5.2), is

$$T_C/T_{\text{RRL}} = 4.3 \times 10^{-5} T_e^{1.15} \Delta\nu_{\text{RRL}} \nu_{\text{RRL}}^{-2.1},$$

where ν_{RRL} and $\Delta\nu_{\text{RRL}}$ denote the RRL frequency (in GHz) and linewidth (in kHz), respectively. Applying this relation, the free-free contribution inferred from $\text{H}40\alpha$ accounts for roughly 70% of the 3 mm flux density, assuming an electron temperature T_e of 10^4 K as reported by Zhang et al. (2023). The Main Core shows that its $\text{H}40\alpha$ has a $\gtrsim 20$ km s $^{-1}$ redshift relative to the HFS systemic velocity traced by $\text{H}^{13}\text{CO}^+ J=1-0$ ($v_{\text{lsr}} \sim 43$ km s $^{-1}$, Fig. 3a4). In contrast, such an offset is not detected in the East Core, although its $\text{H}40\alpha$ is marginally detected (2 σ , see Fig. 3b4).

The unresolved nature of Main Core in ATOMS data motivates the use of higher-resolution QUARKS data to unravel its substructures and kinematics.

4. IONIZED GAS OF THE HC H II REGION

Figure 4a shows the QUARKS 1.3 mm continuum emission associated with the Main Core region, while Figure 4b presents the image after subtracting the CASA-fitted Main Core 1.3 mm component. This subtraction alleviates the contrast issue and clearly reveals extended substructures related to the Main Core, including three prominent morphological features: the arc, the tail, and the cavity. The Main Core has a 1.3 mm integrated flux density of 306 ± 22 mJy, a beam-convolved FWHM of $0.52'' \times 0.44''$, and a deconvolved FWHM of $0.36'' \times 0.3''$ (corresponding to 2170 au \times 1990 au). The 1.3 mm continuum is spatially coincident with $\text{H}30\alpha$ and the hot core dense gas tracer $\text{C}_2\text{H}_5\text{CN } J=26-25$ (234.42396 GHz, $E_u > 100$ K; Liu et al. 2024) line emission in the QUARKS data as shown by Figs. 4c, d and 5, confirming that a HC H II region resides within the hot molecular core—a deeply embedded molecular environment.

4.1. $\text{H}30\alpha$ reconstructed from blended line profile

Owing to the deeply embedded nature of HC H II region, $\text{H}30\alpha$ (231.900928 GHz) is spectrally blended with several narrow lines of molecules at similar frequencies, including HNCO , CH_3OCH_3 , $\text{C}_2\text{H}_5\text{OH}$, CH_3OCHO , and $\text{CH}_3^{18}\text{OH}$. This makes it complicated to accurately derive the spatial distribution and kinematics of the ionized gas. To address this, we employ the eXtended

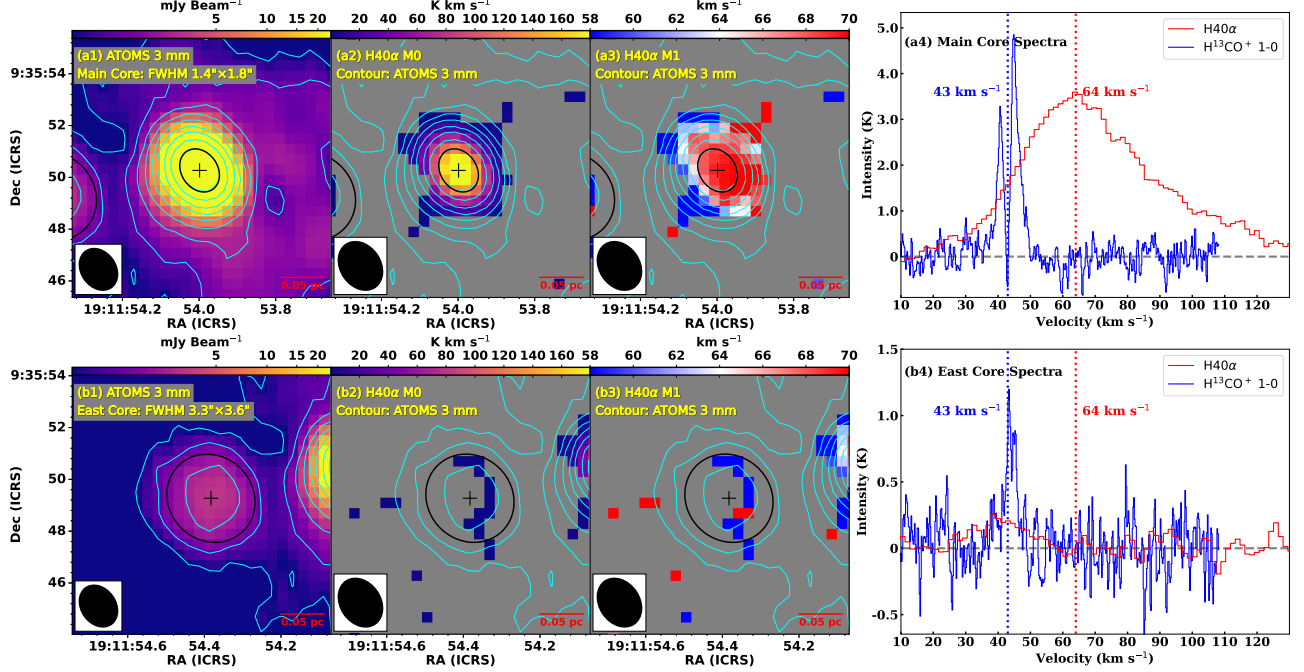


Figure 3. ATOMS 3 mm continuum and H40 α line emission of the Main Core (first row) and the East Core (second row). (a1) 3 mm continuum. (a2) H40 α 0th moment map (a3) H40 α velocity field (1st moment). (a4) Source-averaged H40 α (red) and H¹³CO⁺ (blue) spectra. Panels (b1)–(b4) follow the same order as (a1)–(a4). Contours (levels: 0.72–222 mJy beam^{−1} in 10 logarithmic steps) trace the 3-mm continuum emission. Ellipses denote Gaussian FWHM sizes. All moment maps are generated using 3 σ channel threshold.

CASA Line Analysis Software Suite (XCLASS; Möller et al. 2017) for pixel-by-pixel spectral deblending. XCLASS models molecular and recombination lines, by solving the 1D radiative transfer equation under LTE and isothermal assumptions for H30 α . The details of the deblending process are described in Appendix A.

Panels (a–e) of Fig. 5 display the XCLASS-deblended H30 α maps of electron emission measure (EM), centroid velocity, line width, the source-averaged H30 α and some other molecular line profiles, respectively. The EM map closely mirrors the morphology of the 1.3 mm continuum emission, with its major axis likely following NE–SW direction (Fig. 5a). A global velocity gradient from $v_{\text{lsr}} \approx 64$ km s^{−1} (NE) to $v_{\text{lsr}} \gtrsim 66$ km s^{−1} (SW) is *probably* present in the deblended H30 α centroid velocity map (Fig. 5b). A similar but more pronounced gradient is seen in the H40 α first-moment map, which is redshifted to $v_{\text{lsr}} \approx 70$ km s^{−1} (Fig. 3a3). Both H30 α and H40 α exhibit positive skewness in their line profiles, indicating stronger red wings (Figs. 3a4 and 5d). The H40 α peak velocity becomes increasingly redshifted with larger positive skewness along the NE–SW direction (Appendix B). If the H40 α emission represents a smoothed imprint of the higher-resolution H30 α emission, the true velocity gradient traced by H30 α is expected to be even more significant than shown in Fig. 5b.

The XCLASS deblending assumes a symmetric (Gaussian + Lorentzian) line profile, and therefore asymmetric line wing emission is partly suppressed, leading to an underestimation of the actual velocity gradient. The asymmetric line profiles, as indicated by the positive skewness of H30 α and H40 α , suggest that the ionized flows are anisotropic and deviate from spherical symmetry if both lines are optically thin (Sewilo et al. 2004). Some QUARKS molecular lines (C¹⁸O $J = 2 - 1$, C₂H₅CN $J = 26 - 25$, SiO $J = 5 - 4$) also exhibit positive skewness (Fig. 5e), with SiO and C₂H₅CN can extend up to almost $v_{\text{lsr}} \sim 60$ and 50 km s^{−1}, respectively. The line width of H30 α (Fig. 5c) ranges from 44 to 50 km s^{−1}, consistent with the value of typical HC H II regions (Keto et al. 2008).

4.2. Properties of the HC H II region

From the deblended H30 α EM maps in Fig. 5a, the electron density n_e is estimated as $\sqrt{EM/2R} \sim 2.0 \times 10^5$ cm^{−3} assuming uniform density and FWHM radius R measured from EM map (deconvolved, $0.27'' \times 0.25''$, equivalent to 1560 au). The ionization rate $\dot{N}_i = n_e^2 \alpha_B V \sim 5.4 \times 10^{47}$ s^{−1}, where α_B and V are the Case B total recombination coefficient and HC H II region volume, respectively (Zhang et al. 2024). The derived \dot{N}_i

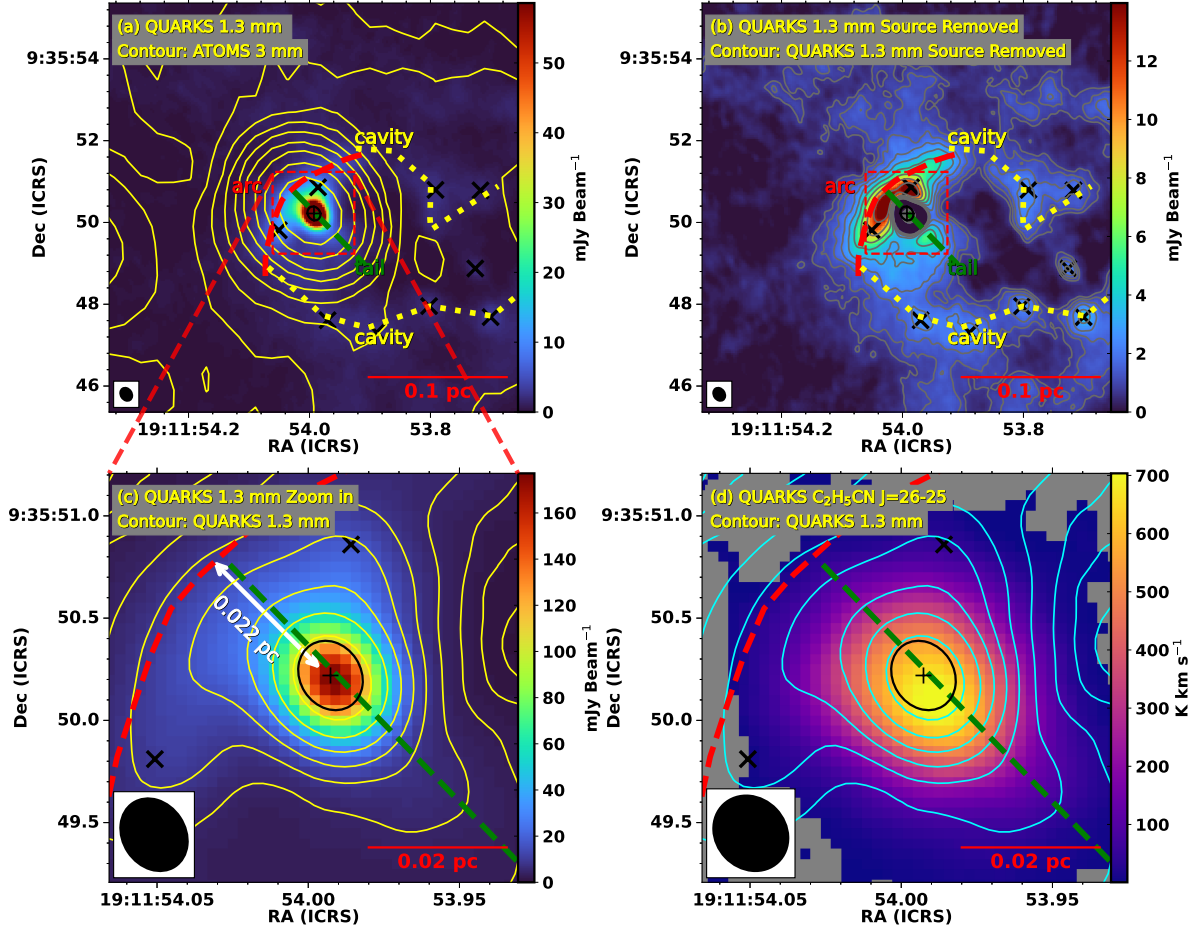


Figure 4. QUARKS images of Main Core and its associated structures. (a) QUARKS 1.3 mm continuum overlaid with ATOMS 3 mm contours (levels identical to Fig. 3) and other extracted 1.3 mm cores (crosses; Jiao et al. in prep.). The extended dusty structures are highlighted with red, green and yellow dashed/dotted lines. (b) QUARKS 1.3 mm continuum after subtracting the CASA-fitted Main Core emission. Associated contour levels are from 6σ to 17.9 mJy beam⁻¹ in 10 logarithmically spaced steps. (c) Zoomed-in view of Main Core in 1.3 mm continuum with contours (levels: 6σ to 0.18 Jy beam⁻¹ in 10 logarithmically spaced steps). The separation between Main Core and arc vertex is indicated with white scalebar. (d) 0th moment map of C₂H₅CN $J = 26 - 25$ overlaid with 1.3 mm contours, tracing hot molecular gas.

corresponds to an ionizing star of type B0.5 to B1 with a mass of $m_* \sim 18 M_\odot$ (Vacca et al. 1996; Keto 2003).

The derived n_e is about an order of magnitude lower than that of typical HC H II regions (Kurtz 2005). Rivera-Soto et al. (2020) identified a number of H II regions in W51A with sizes smaller than 0.01 pc and n_e of 10^4 – 10^5 cm⁻³. They suggested that most of these sources are essentially smaller versions of expanding UC H II regions ionized by early B-type stars, as they follow the extrapolated size– n_e relation established for UC and compact H II regions (Garay & Lizano 1999; Kim & Koo 2001). The I19095 HC H II region shows a similar size, n_e , and ionizing spectral type to those reported by Rivera-Soto et al. (2020), even though it remains deeply embedded within a hot core. Therefore, I19095 likely belongs to the similar class of objects defined by Rivera-

Soto et al. (2020), representing a slightly more evolved stage than typical HC H II regions.

To further constrain the properties of HC H II region, we tested SED models dominated by free-free emission (Fig. 5f) against the archival VLA data spanning 7 mm to 6 cm (see Appendix C; Kurtz et al. 1994; Kavak et al. 2021) plus the free-free contribution of ATOMS 3 mm. Two density profiles were tested: 1) Uniform model: $n_e = n_{e,c}$ ($r < r_c$), yielding $n_{e,c} = 3.2 \times 10^5$ cm⁻³ and $r_c = 1240$ au. 2) Power-law model (Keto 2003): $n_e = n_{e,0} (r/r_0)^{-3/2}$ ($r < r_0$), yielding $n_{e,0} = 0.7 \times 10^5$ cm⁻³ and $r_0 = 1670$ au. Both cases align well with the properties derived from RRL, within a factor of 2. The power-law model predicts a 3 mm flux density consistent with the observations, accounting for approximately 80% of the total 3 mm emission—compatible with the $\sim 70\%$

inferred from the H40 α line. We tested fittings that excluded the 3 mm free-free component and found that the results remain consistent within the uncertainties. Overall, the power-law model provides a better fit than the uniform-density model, suggesting the presence of an electron density gradient within the HC H II region. However, the actual density profile can deviate from the assumed index of $-3/2$, owing to possible departures from spherical symmetry and the limitations of modeling the innermost region (Keto 2003).

The QUARKS 1.3 mm continuum were excluded from the SED analysis due to the heavy contributions from dust emission. After subtracting free-free component in 1.3 mm flux density using the power-law model, the residual 1.3 mm flux density of 162 mJy corresponds to a molecular gas mass of $12 M_{\odot}$ and a surface density of 8.9 g cm^{-2} assuming a T_{dust} of 160 K from Qin et al. (2022), a gas-to-dust ratio of 100 and a dust opacity of $0.9 \text{ cm}^2 \text{ g}^{-1}$ (Ossenkopf & Henning 1994).

5. NATURE OF THE SUPERSONIC IONIZED GAS

The observed velocity shift between the ionized and molecular components is well above the sound speed of the ionized gas $c_i \sim 10 \text{ km s}^{-1}$ (Zhang et al. 2024) and reveals an extremely dynamic system. These spatially correlated components should exhibit distinct interaction signatures. We first describe the extended structures resolved by 1.3 mm in Sect. 5.1 because they can trace the interaction between the ionized gas and the molecular gas and then explore the possible mechanisms driving the supersonic ionized gas in Sect. 5.2.

5.1. Extended structures interacting with HC H II region

The Arc: An arc structure that extends $\sim 0.1 \text{ pc}$ is visible in the 1.3 mm continuum, $\text{C}^{18}\text{O } J = 2 - 1$, and $\text{SiO } J = 5 - 4$ emission, indicated as red dashed lines in both Figs. 4b and 6. The continuum-traced arc appears slightly further from the HC H II region and encloses the arc traced by C^{18}O and SiO . The arc vertex lies $0.022 \text{ pc } (0.75'' \pm 0.1'')$ from the center of the HC H II region. The arc mass is around 30 to $90 M_{\odot}$, estimated with a 1.3 mm flux density of 0.11 Jy and a T_{dust} of 50 to 20 K. Position-velocity diagrams (PVDs) along the arc for C^{18}O and SiO are shown in Fig. 6. The C^{18}O PVD displays a parabolic shape, also evident in several QUARKS molecular lines (SO , ^{13}CS , CH_3OH , CH_3CN , and H^{13}CN ; see Appendix D). Fitting a parabola to the velocity of the emission peak in each position for C^{18}O PVD yields a vertex velocity of $\sim 40 \text{ km s}^{-1}$ and end velocities between 43 and 45 km s^{-1} . In contrast, SiO does not clearly show this characteristic of a parabolic shape

velocity, but rather exhibits a more consistent velocity around 43 km s^{-1} .

The Tail: Extending $\sim 0.044 \text{ pc}$ from the HC H II region center to the southwest, the tail approximately aligns with the arc symmetry axis and the most redshifted regions of HC H II region (Figs. 3a3 and 5b). The PVDs along the tail axis for C^{18}O and SiO (Figs. 6c1 and c2) reveal very high-velocity red line wings extending beyond $v_{\text{lsr}} \approx 50 \text{ km s}^{-1}$ and $v_{\text{lsr}} \approx 60 \text{ km s}^{-1}$, respectively, at the position corresponding to the HC H II region (offset $\sim 0.75''$). Figure 7 shows the channel map of $\text{SiO } J = 5 - 4$, with a channel width of 2.4 km s^{-1} . The first-order moment maps of C^{18}O and SiO clearly show that the arc structure is blueshifted relative to the redshifted tail originating from the position of the HC H II region. The tail can still be seen up to $v_{\text{lsr}} \sim 60 \text{ km s}^{-1}$ in the channel map, indicating that the tail in the continuum is dominated by the high-velocity shocked molecular gas.

The Cavity: A cavity-like structure, characterized by 1.3 mm, C^{18}O , and SiO emission, is outlined in Figs. 4 and 6 by the yellow dotted lines. Its edge is spatially associated with several faint low-mass cores with individual masses \lesssim a few solar masses and total mass $\lesssim 24 M_{\odot}$ when assuming a T_{dust} of 20 K. These cores are identified using the source extraction algorithm `getsf` (Men'shchikov 2021) by Jiao et al. in preparation. The two low-mass cores that account for only about 9% of the arc flux density appear near the arc vertex, and therefore they are weak compared to the bright extended arc.

5.2. Powering mechanism of the supersonic ionized gas

In this section, we explore three possible origins of supersonic ionized gas by examining their compatibility with the observational signatures.

Trapped Collapsing Ionized Region: Within an extremely dense HC H II region, a bounded structure and accretion of ionized gas could be achieved due to strong gravity, as proposed by Keto (2003). A large RRL optical depth accompanying the non-LTE effect would produce a net red-shifted profile for RRLs (Peters et al. 2012; Klaassen et al. 2018).

However, this scenario is unlikely for our target. First, the HC H II region is too large for gravitational confinement. The maximum radius for a gravitationally trapped HC H II region, given by $r_{\text{max}} = Gm_*/2c_i \sim 60 \text{ au}$ (where m_* is mass of ionizing star; Keto 2003), is significantly smaller than the observed size of 1560 au. Second, both H30 α and H40 α lines remain optically thin at $n_e \sim 10^5 \text{ cm}^{-3}$ and the size scale of HC H II region. The optical depths of the RRL and the free-free contin-

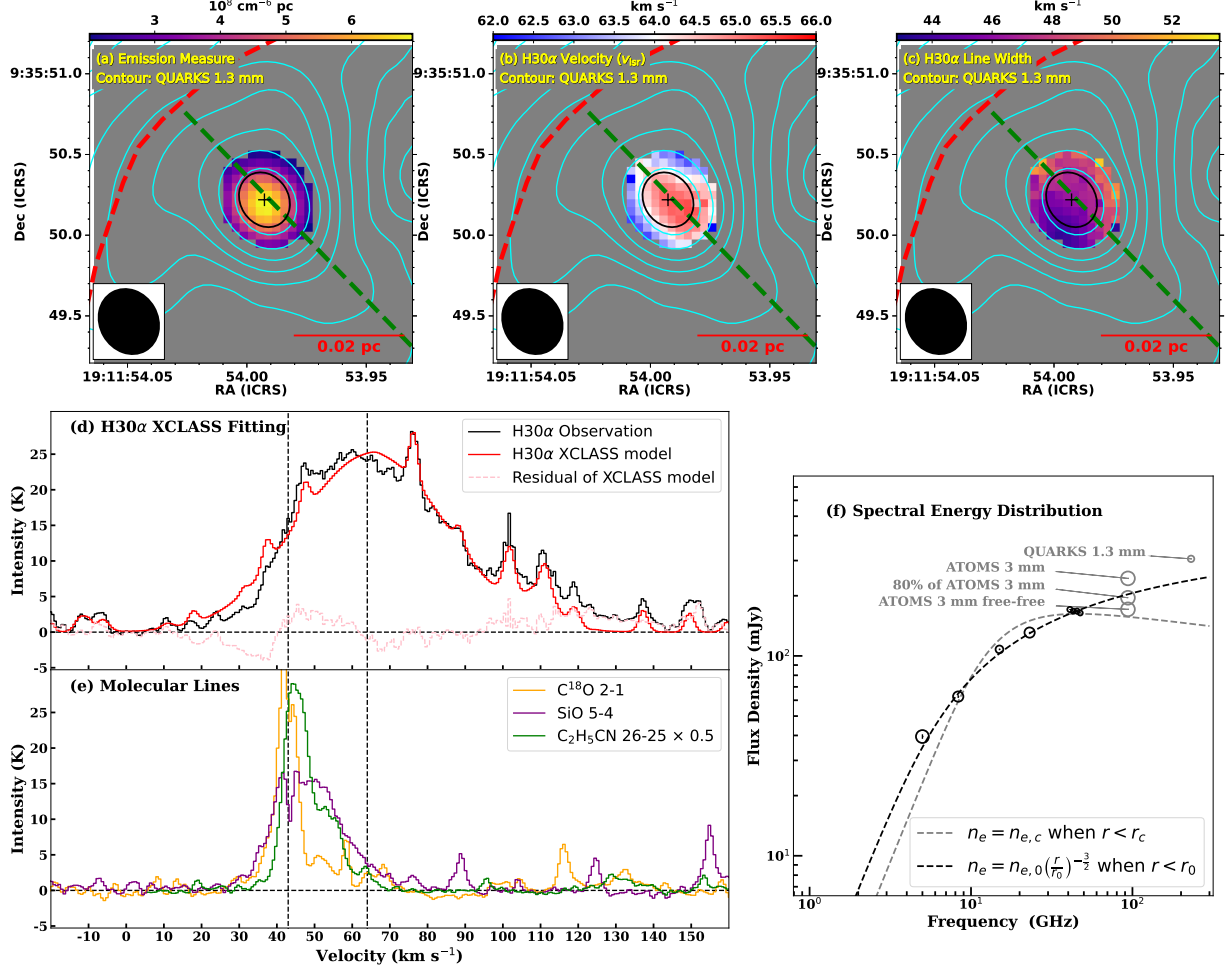


Figure 5. XCLASS-deblended H30 α . (a) EM, (b) centroid velocity, and (c) line width. (d, e) source-averaged spectra: observed (black) and modeled (red) H30 α , compared with C¹⁸O, C₂H₅CN, and SiO. The observed and modeled H30 α spectra both include the molecular line emission. (f) SED fitted with uniform (gray) and power-law (black) density models. Archival VLA data (7 mm–6 cm; Appendix C) and ATOMS 3 mm/QUARKS 1.3 mm data are shown as black and gray dots, respectively, with sizes indicating the beam size of observations.

uum are given by:

$$\tau_{\text{RRL}} \sim 1.9 \times 10^3 \left(\frac{T_e}{\text{K}} \right)^{-5/2} \left(\frac{EM}{\text{cm}^{-6} \text{ pc}} \right) \left(\frac{\Delta\nu_{\text{RRL}}}{\text{kHz}} \right)^{-1}$$

$$\tau_{\text{ff}} \sim 3.3 \times 10^{-7} \left(\frac{T_e}{10^4 \text{ K}} \right)^{-1.35} \left(\frac{EM}{\text{cm}^{-6} \text{ pc}} \right) \left(\frac{\nu_C}{\text{GHz}} \right)^{-2.1},$$

where ν_C is the continuum frequency (Wilson et al. 2013; Condon & Ransom 2016). Both values are < 0.015 for the targeted source. Non-LTE effects, such as pressure broadening, are negligible, as evidenced by the near-zero ratio of the Lorentzian line width to the thermal line width in frequency $\Delta\nu_L/\Delta\nu_{\text{therm}} = 1.2(n_e/10^5 \text{ cm}^{-3})(N/92)^7 \sim 0.007$, for $N = 40$ and $n_e \sim 2 \times 10^5 \text{ cm}^{-3}$ (Keto et al. 2008).

Using RADMC-3D non-LTE radiative transfer code (Dullemond et al. 2012), we model an infalling isother-

mal HC HII region with a power-law density distribution $n_e \propto r^{-3/2}$ derived from SED fitting in Sect. 4.2 (details in Appendix E). An infall velocity of $v_{e,0}^{\text{infall}} = c_1$ is adopted at its outer boundary, following Keto (2003), which assumes that the boundary corresponds to an R-critical jump where the ionized gas leaves the front at c_1 . The modeled RRLs fail to reproduce the observed 20 km s⁻¹ global velocity shift. We therefore conclude that a gravitationally bound, infalling ionized region is unlikely and that the shift reflects the actual kinematics of the ionized gas without significant bias from the optical effect.

Bow Shock of a Runaway High-Mass Star: In this scenario, a high-mass star moves supersonically through its surrounding cloud. When the momentum flux in the stellar wind equals the ram pressure of the ambient medium, a bow-shaped ionized shock front is created

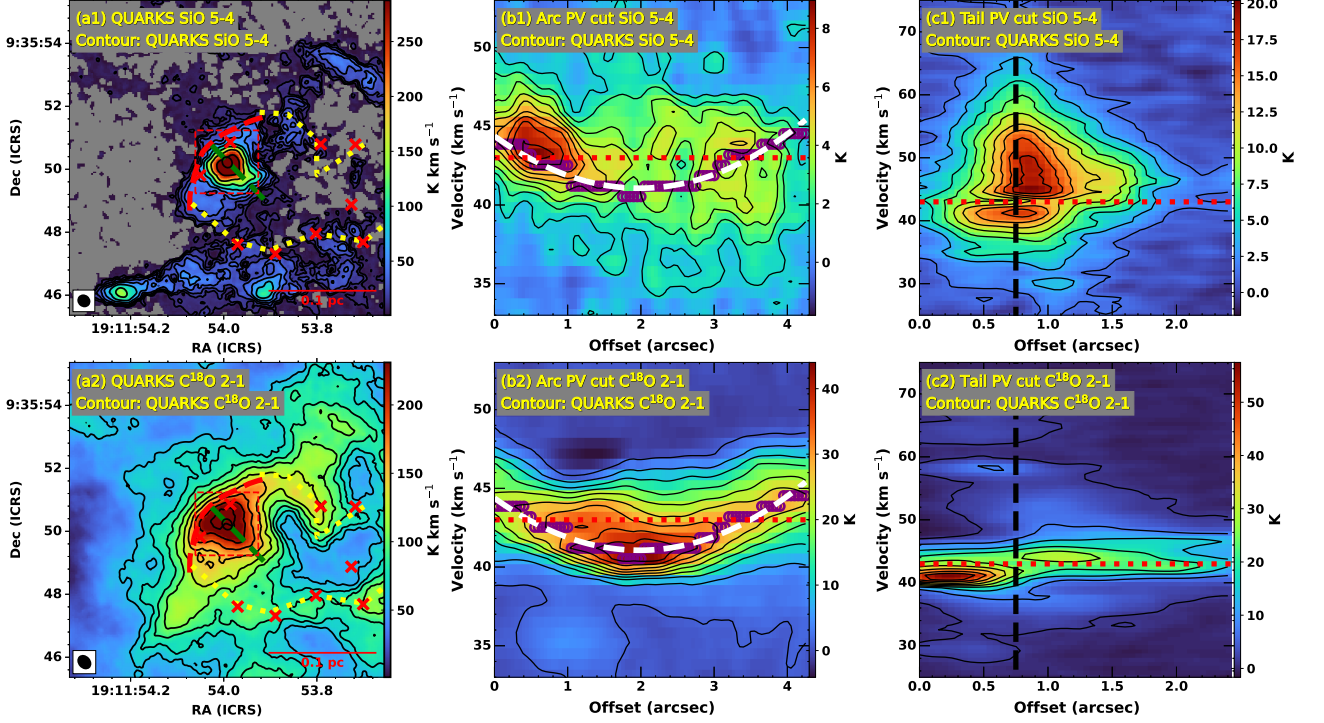


Figure 6. Molecular gas of extended structures. (a1, a2) 0th moment maps with 3σ channel cutoff of SiO $J = 5 - 4$ and $C^{18}O$ $J = 2 - 1$ emission, overlaid with 10 logarithmic contours from 9 to 432 K km s⁻¹ for SiO and from 60 to 306 K km s⁻¹ for $C^{18}O$. (b1, b2, c1 and c2) PV diagrams of SiO and $C^{18}O$ along arc and tail, respectively (contour levels: 3σ to 8.9 K [b1], 44 K [b2], 20.2 K [c1] and 57.5 K [c2] in 10 linear steps). Dotted horizontal lines indicate the systemic velocity of the hub whereas the vertical dashed line in panels c1 and c2 indicate the center position of HC H II region. Purple dots and dashed parabolic curve in panels b1 and b2 mark the peak $C^{18}O$ velocity positions and their best-fit parabola.

ahead of the motion direction of the star and comoving with the star. Such runaway stars originate from either binary companion supernovae or cluster dynamical ejection (Fujii & Portegies Zwart 2011; Rodríguez et al. 2020). Although the arc detected in 1.3 mm continuum and molecular emission ($C^{18}O$ and SiO) would initially suggest a bow shock from a runaway high-mass star and associated comoving ionized gas as the mechanism of supersonic ionized gas, we disfavor this interpretation for the following two reasons.

First, the observed velocity structure disagrees with the theoretical expectations. In the bow-shock scenario, the velocity of the ionized gas near the vertex should match stellar velocity v_* , as the ionization front becomes trapped in the swept-up shell behind the bow shock formed ahead of the moving star (Arthur & Hoare 2006). In contrast, ionized gas in the trailing regions is expected to approach the ambient velocity due to deceleration and mixing with the surrounding medium (van Buren & Mac Low 1992; Zhu et al. 2008). Assuming that v_* equals the RRL velocity at the position closest to the arc vertex ($v_{\text{lsr}} \approx 64$ km s⁻¹), the observed ionized-gas kinematics—appear redder toward the tail—seen in Figs. 3a3 and 5b is inconsistent with this prediction,

since the tail should exhibit velocities closer (bluer) to the ambient molecular gas. A more reliable evidence is the molecular gas kinematics because it is fully resolved. The bow-shock model predicts that molecular gas near the vertex should show velocities closest to v_* , where the stellar wind imparts the greatest momentum along the direction of motion (Wilkin 1996; Zhu et al. 2015). However, the parabolic velocity structure in the $C^{18}O$ PVD (Fig. 6b2) instead reliably reveals a blueshifted vertex relative to other parts of the arc—opposite to the model prediction.

Second, the stand-off distance is unlikely to be compatible with observations. The separation between the ionizing star and bow vertex derived from momentum conservation, known as the stand-off distance, is given by

$$d_{\text{so}} = \sqrt{\dot{m}_w v_w / 4\pi \rho v_*^2},$$

where \dot{m}_w and v_w are the stellar wind mass loss rate and terminal velocity, and ρ is the ambient gas density (Wilkin 1996). Adopting extreme parameters corresponding to an unusually strong stellar wind ($\dot{m}_w = 10^{-5} M_\odot \text{ yr}^{-1}$, $v_w = 3000$ km s⁻¹; Kudritzki & Puls 2000; Vink et al. 2001) and a lowest ambient den-

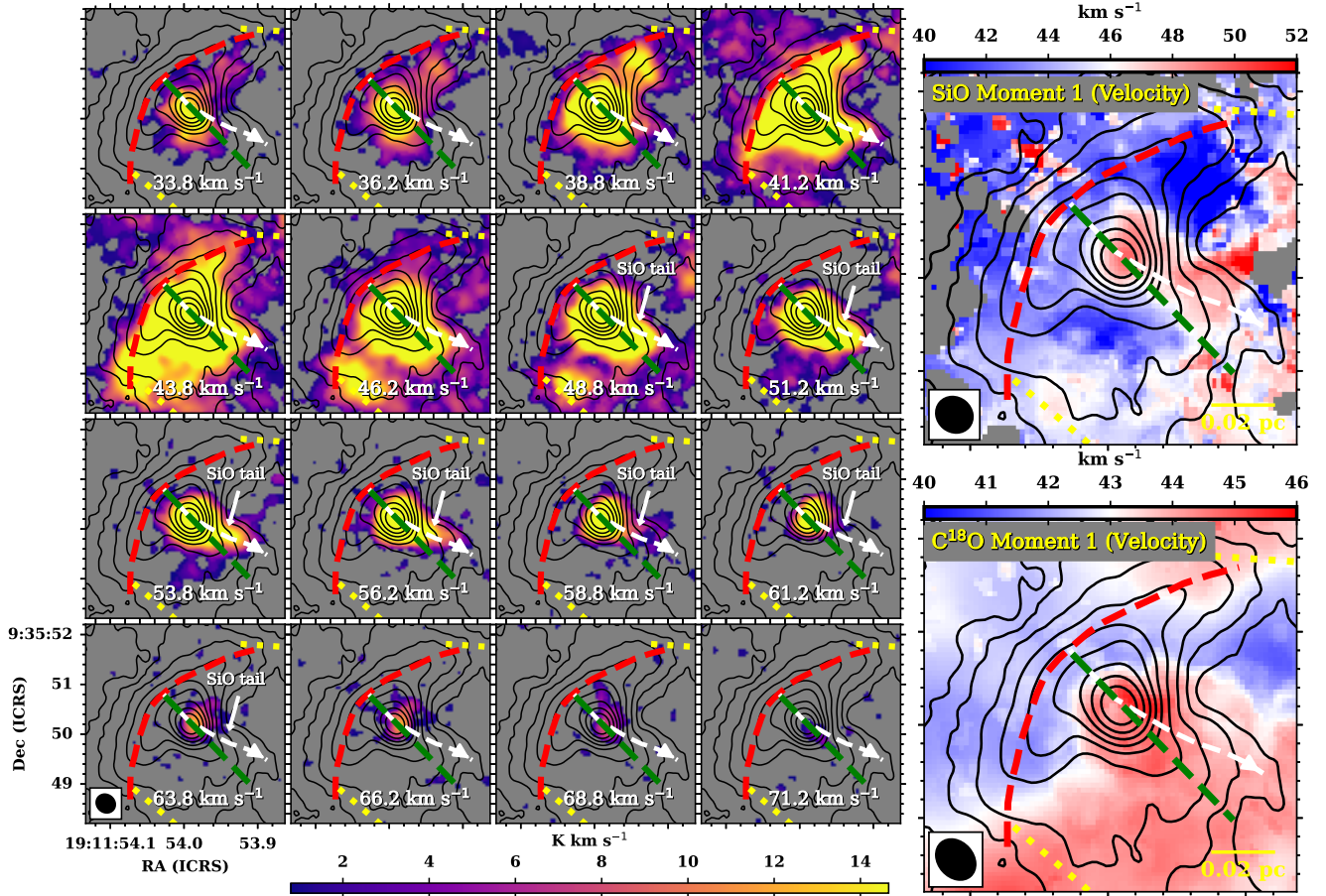


Figure 7. Channel map of SiO $J = 5 - 4$ (left panels) and the first order moment maps of SiO $J = 5 - 4$ and C¹⁸O $J = 2 - 1$ (right panels). Black contours show 1.3 mm continuum emission, with levels the same as Fig. 4. The high-velocity SiO tail is highlighted with white arrows.

sity ($n_{\text{H}} = 3 \times 10^5 \text{ cm}^{-3}$) corresponding to clump-scale density derived from ATLASGAL (Urquhart et al. 2022), the resulting maximum stand-off distance is $d_{\text{so}} \sim 0.024 \text{ pc}$, close to the observed separation of 0.022 pc . However, in reality stellar winds are expected to be much weaker and the ambient density much higher, which reliably rules out a bow-shock origin for the arc. For example, a more reasonable parameter set of $\dot{m}_{\text{w}} = 10^{-6} M_{\odot} \text{ yr}^{-1}$, $v_{\text{w}} = 2000 \text{ km s}^{-1}$ (Zhang et al. 2024), and $n_{\text{H}} = 10^6 \text{ cm}^{-3}$ (typical of a dense core) yields only $d_{\text{so}} \sim 0.003 \text{ pc}$.

Champagne Flow Breaking Out of a Hot Molecular Core: Having rejected both the bow shock and infalling ionized gas scenarios, we consider the champagne flow model where a stationary or slowly moving ionizing star drives supersonic ionized flows along density gradients, producing the observed global velocity shift. This model provides a better explanation for the observed kinematics. The arc structure is plausibly formed through compression of a pre-existing filament (likely embedding two low-mass cores) by the expanding HC H II region, where

expansion toward the filament is severely inhibited by an upward density gradient. The expansion toward the upward density gradient tends to produce a parabolic density structure such as the exemplar shown in Zhu et al. (2015). It is worth noting that two dense cores are likely located on either side of the arc’s vertex, suggesting that they may further constrain the direction of the expansion. The slow expansion (~ 2 to 3 km s^{-1}) produces the parabolic velocity structure with a blueshifted vertex ($v_{\text{lsr}} \sim 40 \text{ km s}^{-1}$) in the C¹⁸O PVD (Fig. 6b2), and powers the narrow SiO shock emission (width $\sim \text{few km s}^{-1}$) observed around the clump velocity in the arc. In the opposite direction, a steep downward density gradient along the tail direction (from hot core to inter-core cavity shown in Fig. 4) enables ionized gas to flow outward at several times the sound speed c_i , creating global redshifted emission (Tenorio-Tagle et al. 1979). A density contrast with a factor of a few hundred can create a maximum flow velocity of $3c_i$ to $4c_i$ (Tenorio-Tagle 1979). The outflowing ionized gas entrains or sweeps up the ambient molecular material, producing

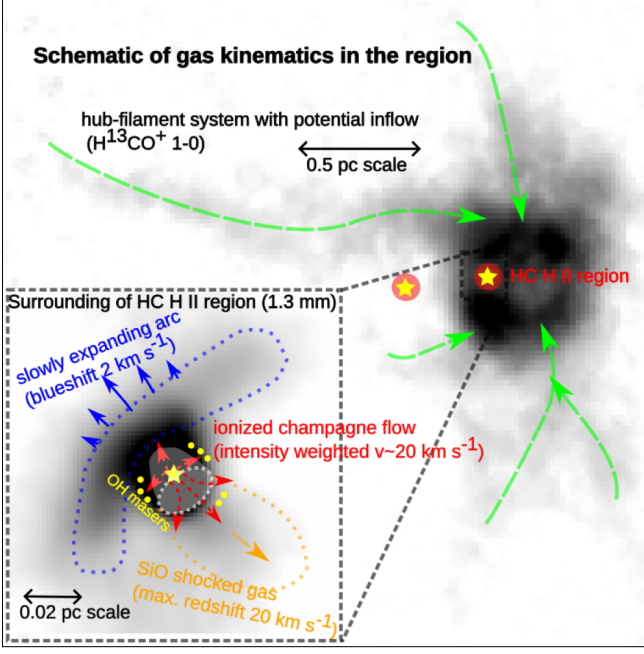


Figure 8. Schematic for the flows related with the HC H II region in this work.

the redshifted high-velocity SiO shocked tail detected up to $v_{\text{lsr}} \sim 60 \text{ km s}^{-1}$ on the channel map (Fig. 7). Supporting evidence for the flow direction includes a possible velocity gradient in the RRL emission and the continuum/SiO tail observed along the NE–SW direction. This “confined slow expansion in the head plus an accelerating champagne flow in the tail” pattern, is reproduced in numerical simulations (Bodenheimer et al. 1979; Tenorio-Tagle et al. 1979; Arthur & Hoare 2006; Zhu et al. 2015), particularly when stellar winds assist expansion. Figure 8 schematically illustrates this mass flow pattern for the I19095 HC H II region.

OH masers provide critical insight into the HC H II region–ambient gas interactions, tracing compressed shells between the fronts of ionization and shock (Elitzur & de Jong 1978; Fish & Reid 2007). VLBA observations at 15 mas resolution show OH masers enveloping the HC H II region with $v_{\text{lsr}} = 39$ to 47 km s^{-1} , delineating a dense interface shell as shown in Fig. 9 (Fish et al. 2005). Critically, masers show no concentration around the arc, strongly disfavoring the bow shock model, which predicts maximal interaction in the bow structure and thus the highest probability of OH maser detection there (Gasprong et al. 2002).

Given that QUARKS observations lack the resolution to probe the internal structure of the HC H II region whose size is partly evidenced by the OH maser distributions, constructing detailed morphological/kinematic models and performing comprehensive radiative trans-

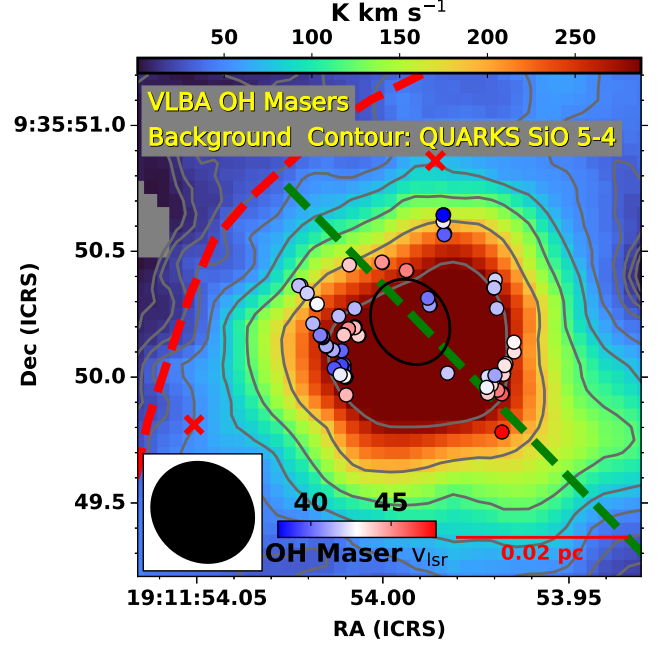


Figure 9. OH masers detected with the VLBA by Fish et al. (2005), color-coded by their v_{lsr} . The background colormap represents a zoomed-in view of the QUARKS SiO $J = 5 - 4$ first-moment map shown in Fig. 6a1.

fer calculations (Dullemond et al. 2012; Peters et al. 2012) for comparison with H30 α observations would be overly speculative. Instead, we only test whether the global 20 km s^{-1} shift of the RRL can be reproduced by a simplified champagne flow toy model. Following Keto et al. (1995), we define the ionized flow velocity, density, and cross-sectional area at position z as $v_e(z) = v_{e,0}^{\text{flow}} (z/z_0)^{-\alpha_v}$, $n_e(z) = n_{e,0}^{\text{flow}} (z/z_0)^{-\alpha_n}$, and $A(z) = A_0^{\text{flow}} (z/z_0)^{-\alpha_A}$, respectively, with mass conservation requiring $\alpha_v + \alpha_n + \alpha_A = 0$ ($\alpha_A < 0$, $\alpha_v < 0$). In unresolved observations, the optically thin RRL profile is the integration of emission along the flow:

$$I(v) \propto \int n_e^2(z) A(z) \phi(v_c = v_e(z), \sigma_e) dz,$$

where ϕ is the Gaussian profile centered at $v_e(z)$ with dispersion σ_e . Transforming to velocity space yields the following:

$$I(v) \propto \int_0^{v_{e,\text{max}}} v_e^{(\alpha_n - 2\alpha_v - 1)/\alpha_v} \phi(v_c = v_e, \sigma_e) dv_e.$$

We explore parameter grids: $|\alpha_v|, \alpha_n \in [0.2, 3.0]$ with 0.025 step, $\sigma_e \in [12, 25] \text{ km s}^{-1}$ and $v_{e,\text{max}} \in [40, 80] \text{ km s}^{-1}$ with 1 km s^{-1} step. Models with a coefficient of determination $R^2 > 99.999\text{th}$ percentile across all model grids shown in Fig. 10 reproduce well the 20 km s^{-1} global red shift and blue parts of the line

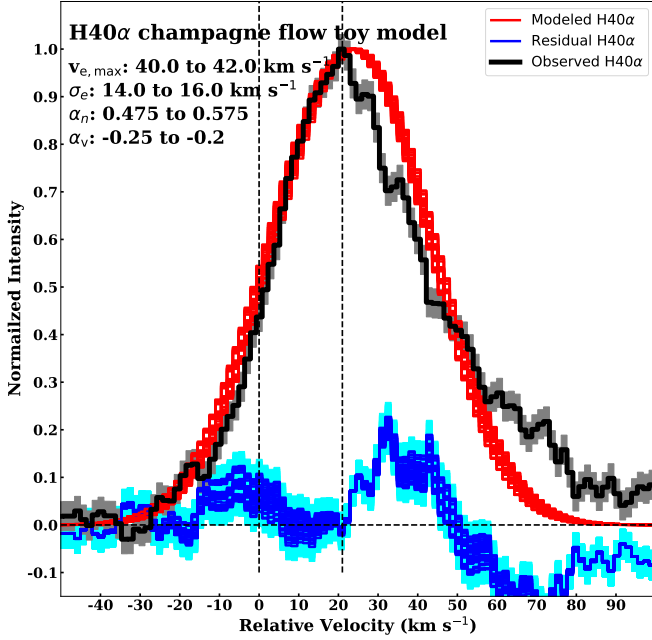


Figure 10. Comparison of the observed H40 α line profile (black; gray shading indicates 1σ error) with the prediction of toy models of champagne flow (red). The residuals (model minus observation) are shown in blue, with cyan shading indicating the 1σ uncertainties.

profile. This toy model demonstrates the *feasibility* of champagne flow origins for the global velocity shift, although it is not a fully complete model that can be comprehensively compared with observations. Deviations occur in the red wing, possibly due to over-simplified kinematics, mass distribution, and morphology. For instance, excess emission at relative velocity $> 60 \text{ km s}^{-1}$ is likely associated with unmodeled high-velocity components beyond $v_{e,\text{max}}$, while the deficit at $20\text{--}40 \text{ km s}^{-1}$ likely indicates a central wind-cleared cavity with low density and velocity.

6. HATCHING OUT OF THE EGG PHASE AND CONCLUSIONS

We evaluated three scenarios for the global supersonic velocity shift in the optically thin RRLs of I19095 HC H II region and concluded that a champagne flow represents the most plausible mechanism. The HC H II region remains deeply embedded within a 0.02 pc -scale hot molecular core, indicating that we are observing a rapid “hatching out of the egg” transition phase in the evolution of the hot core–HC H II region: the ionized gas has just broken out of the parental hot core and flows supersonically into the lower-density inter-core region of the clump. The potential inclination of the flow implies a global velocity $> 20 \text{ km s}^{-1}$. The slightly more evolved nature of the low-density HC H II regions proposed by

Rivera-Soto et al. (2020) is consistent with the interpretation that the I19095 HC H II region is undergoing the “hatching” phase, resulting in its lower electron density compared to the more embedded, hyperdense HC H II regions.

In subsequent evolution, the ionization front is expected to expand supersonically into the inter-core regions within the clump and form an irregular UC H II region, accompanied with flow deceleration, which will diminish the global velocity shift and thus make the detection window of “hatching” phase extremely brief. The rarity of supersonic velocity shifts among HC H II regions (1/16 in the ATOMS survey; red dots in Fig. 1c) reflects that the short duration of this phase likely constitutes $< 10\%$ of the typical HC H II region lifetime. Since these supersonic flows precede the formation of UC H II regions, the “hatching” phase must be much shorter than the typical UC H II region lifetime of $\sim 3 \times 10^5 \text{ yr}$ (Wood & Churchwell 1989; Churchwell 2002; Mottram et al. 2011; Kalcheva et al. 2018). Therefore, the maximum timescale of the “hatching” phase, estimated by combining the UC H II region lifetime with the number ratio of supersonic HC H II regions to all HC H II regions in the ATOMS sample (1/16), is approximately $1/16 \times 3 \times 10^5 \approx 2 \times 10^4 \text{ yr}$. Meanwhile, using the ratio of supersonic HC H II regions to all compact (UC + HC H II) regions with radii $< 0.05 \text{ pc}$ (1/63), the typical timescale of the “hatching” phase is about $1/63 \times 3 \times 10^5 \approx 5 \times 10^3 \text{ yr}$. Given that the Galactic OB star formation rate is around 0.01 to 0.05 per year, only tens of HC H II regions in such “hatching” phase probably exist in the Galaxy today, highlighting the extreme difficulties in detection of such exotic HC H II regions (Reed 2005; Robitaille & Whitney 2010; Chomiuk & Povich 2011).

Although extremely short compared to the HMSF timescales, this phase—and its associated supersonic champagne flow—should prevail during the transitions from HC H II regions embedded in hot cores to UC H II regions (Kim & Koo 2001). This prevalence stems from the inherent anisotropic density distributions within the parental hot cores and their surroundings, as demonstrated in the DIHCA project (Digging into the Interior of Hot Cores with ALMA; Olguin et al. 2021, 2022, 2023). Such anisotropy naturally drives gradient-driven champagne flows. Asymmetric expansion beginning at the HC H II region stage complicates the expansion process and contributes to the lifetime-dynamical time discrepancy in UC H II region (Wood & Churchwell 1989; Kim & Koo 2001).

Stellar winds significantly influence early H II region kinematics (Geen et al. 2021). Simulations show that

winds combined with density gradient-driven champagne flows produce cavities and complex velocity structures (Arthur & Hoare 2006). Our ~ 2000 au resolution QUARKS data cannot resolve the inner structure of I19095 HC H II region, and discrepancies between continuum SED fitting and RRL modeling power-law indices likely arise from differing morphological assumptions and wind-induced complexity.

We advocate for future searches for the supersonic HC H II region coupled with long baseline ALMA observations resolving to ~ 100 au scales, to map the gas dynamics during this critical and rapid transient phase.

SZ gratefully acknowledges support by the CAS-ANID project CAS220003. GG and LB gratefully acknowledge support by the ANID BASAL project FB210003. AS gratefully acknowledges support by the Fondecyt Regular (project code 1220610), and ANID BASAL project FB210003. This research was carried out in part at the Jet Propulsion Laboratory, which is operated by the California Institute of Technology under a contract with the National Aeronautics and Space Administration (80NM0018D0004). We want to thank the anonymous referee for the constructive comments that helped to improve the quality of the paper.

This paper makes use of the following ALMA data: ADS/JAO.ALMA#2019.1.00685.S, 2021.1.00095.S and 2023.1.00425. ALMA is a partnership of ESO (representing its member states), NSF (USA), and NINS (Japan), together with NRC (Canada), MOST and ASIAA (Taiwan), and KASI (Republic of Korea), in cooperation with the Republic of Chile. The Joint ALMA Observatory is operated by ESO, AUI/NRAO, and NAOJ.

Facilities: ALMA.

Software: `astropy` (Astropy Collaboration et al. 2022), `CASA` (CASA Team et al. 2022), `FilFinder` (Koch & Rosolowsky 2015), `XCLASS` (Möller et al. 2017), `RADMC-3D` (Dullemond et al. 2012).

APPENDIX

A. H30 α LINE DEBLENDING

The philosophy of H30 α line deblending is to remove the overlapping molecular lines by fitting their multiple transitions outside the H30 α frequency range. Our general workflow includes three steps: line identification, XCLASS model fitting, and individual line reproduction.

First, we select the northern arc where complex organic molecules are abundant while H30 α is absent. Based on the CDMS database¹, we have identified molecular species with more than one transitions: $^{13}\text{CH}_3\text{CN}$, CH_3OH , $\text{CH}_3^{18}\text{OH}$;A/E, CH_3CHO ;v=0, CH_3OCHO ;v18=1, $\text{C}_2\text{H}_5\text{OH}$, $\text{CH}_3\text{C}^{15}\text{N}$, $\text{C}_2\text{H}_5\text{CN}$, CH_3OCH_3 , SO_2 ;v2=1, and HC(O)NH_2 . In addition, there are five species with only one transition: ^{13}CS , OCS , t-HCOOH , and HNCO . By fitting observations with the `myXCLASSFit` algorithm, we obtain a template model for further fitting.

Then, we add H30 α to the model, which can be described by one kinematic component characterized by source size, T_e , electron EM, Gaussian Δv_G and Lorentzian Δv_L line width contributions, and velocity offset v_{off} . In the region with strong H30 α detection, we then apply the model to fit the spectra pixel by pixel with `myXCLASSMapFit`. As an example, we show a successfully fitted spectrum in Fig. 11.

Finally, we retrieve the individual model H30 α to reproduce the RRLs in each pixel. The fitted EM, centroid velocity and line width are shown in Fig. 5(a-c).

¹ <https://cdms.astro.uni-koeln.de/>

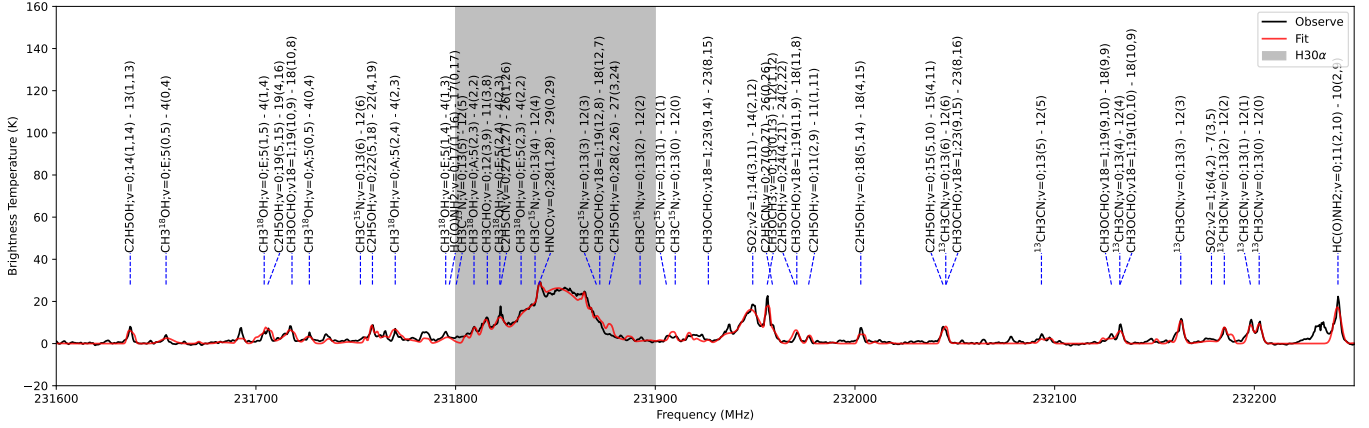


Figure 11. Example of successfully fitted spectrum towards the 1.3 mm peak where the HC H II region is located. Black and red lines are the observed and fitted spectra. Gray shade highlights the frequency range of H30 α .

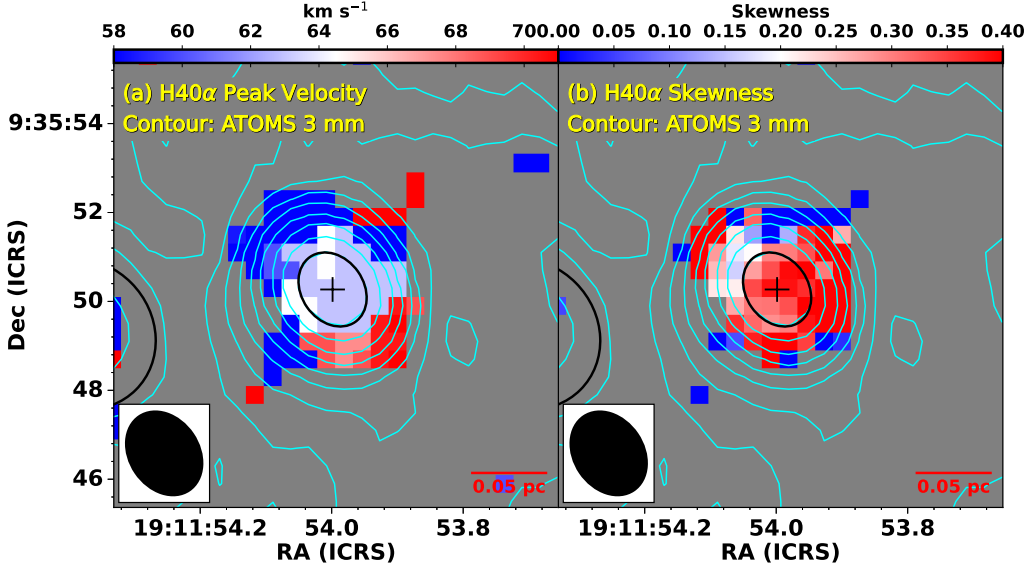


Figure 12. Peak velocity and skewness maps for H40 α , overlaid with ATOMS 3 mm emission contours with levels the same as Fig. 3.

B. H40 α LINE PROFILE

Figure 12 shows the maps of the peak velocity and skewness for H40 α . Global changes along the NE-SW direction are obvious.

C. SED FITTING

The SED fitting methodology follows Keto (2003), modeling free-free emission from a spherical HC H II region as:

$$S_\nu = \frac{4\pi k_B T_e \nu^2}{c^2} \int_0^{\theta_0} \theta (1 - e^{-\tau_{ff}}) d\theta, \quad (C1)$$

where $\theta = \sqrt{x^2 + y^2}/D$ is the angular sky coordinate and $\tau_{ff}(T_e, EM, \nu)$ denotes the frequency-dependent free-free optical depth (Sect. 5.2). Varying electron density profiles produce distinct SED shapes. We adopt $T_e = 10^4$ K and fit both uniform-density and power-law ($n_e \propto r^{-3/2}$) models, employing the simplifications detailed in Keto (2003). The fitting incorporates archival VLA data spanning 7 mm to 6 cm:

7 mm: Observations of I19095 were conducted in the VLA B-configuration at Q-band (Project ID: 23A-205; PI: Fengwei Xu). The WIDAR correlator provided 8 GHz continuum coverage centered at 44 GHz. After manual calibra-

tion in CASA 6.5.4, four sub-band images were generated at 41.0, 43.1, 45.4, and 47.5 GHz, enabled by the upgraded correlator. Self-calibration improved the image quality, yielding a synthesized beam of $\sim 0.25'' \times 0.18''$ and an image rms noise of ~ 0.4 mJy beam $^{-1}$. The measured flux densities are 170.7 ± 2.1 , 167.3 ± 1.5 , 167.6 ± 1.8 , and 164.0 ± 1.8 mJy, respectively, with a source size of $\sim 0.2'' \times 0.16''$.

1.3 cm & 6.0 cm: Data from Kavak et al. (2021) (B-configuration; *K*- and *C*-bands) yield flux densities of 130.87 ± 2.60 mJy and 39.50 ± 1.60 mJy, respectively. The synthesized beam sizes are $0.91'' \times 0.84''$ and $1.49'' \times 1.28''$, with corresponding source sizes of $0.34'' \times 0.23''$ and $1.18'' \times 0.26''$, respectively.

2.0 cm & 3.6 cm: Archival B-configuration data from Kurtz et al. (1994) provide flux densities of 107.8 ± 1.8 mJy and 62.6 ± 0.6 mJy. The synthesized beam sizes are $0.54'' \times 0.46''$ and $1.02'' \times 0.77''$, with source sizes of $0.6'' \times 0.5''$ and $1.1'' \times 0.9''$, respectively.

D. POSITION-VELOCITY DIAGRAMS ALONG THE ARC

Figure 13 shows additional PVDs of several QUARKS molecular lines. The C^{18}O -fitted parabola matches the velocity structures well, strongly supporting the existence of parabolic kinematics.

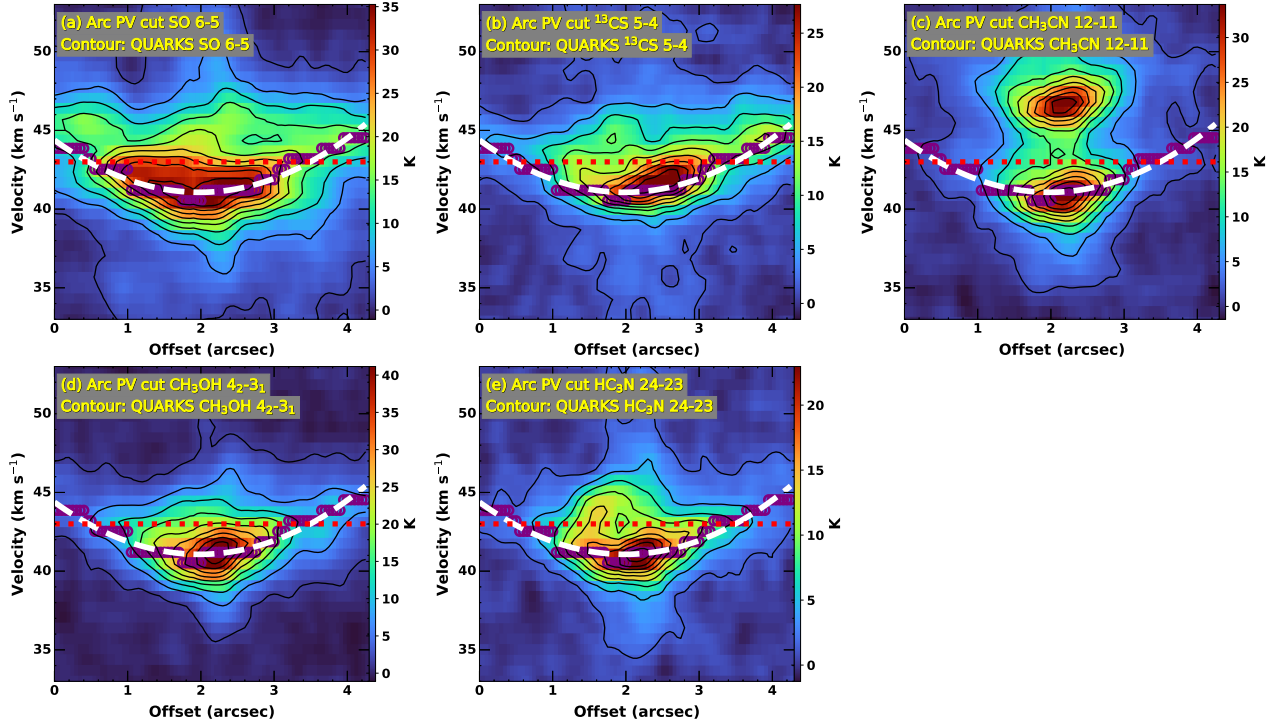


Figure 13. Position-velocity diagrams along the arc. Panels (a)-(e) show the PVDs of SO 6 – 5, ^{13}CS 5 – 4, CH_3CN 12 – 11, CH_3OH 4₂ – 3₁, and HC_3N 24 – 23, respectively. Contours run from 3σ to 37.2, 30.6, 36.3, 47.3, and 28.2 K in 10 linear steps, respectively. Other labels and lines are as in Fig. 6.

E. RADMC-3D MODELING OF AN INFALLING HC H II REGION

With the non-LTE radiative transfer code RADMC-3D specifically modified for RRLs by Peters et al. (2012), we modeled H30 α lines of an HC H II region using power-law density and velocity distributions consistent with mass conservation: $n_e = n_{e,0}^{\text{infall}} (r/r_0)^{-3/2}$ ($r_i < r < r_0$) and $v_e = -v_{e,0}^{\text{infall}} (r/r_0)^{-1/2}$ ($r_i < r < r_0$). The outer radius $r_0 = 1650$ au and the density $n_{e,0}^{\text{infall}} = 0.7 \times 10^5$ cm $^{-3}$ were adopted from the free-free SED fitting results. We set the radius of the density plateau to $r_i = r_0/50 \sim 33$ au. The infall velocity at the outer boundary of HC H II region, $v_{e,0}^{\text{infall}}$, was assumed to be the sound speed c_1 . The model utilized a 3D grid of $150 \times 150 \times 150$ cells with 10^6 photons packages and a constant $T_e = 10^4$ K. Figure 14 presents the resulting 0th and 1st moment maps, along with the spatially averaged spectra over the entire HC H II region and four subregions. While the source-averaged H30 α line exhibits an asymmetric profile, primarily due to emission from the innermost pixels (Region 0), the model H30 α lines show no significant redshift,

except for the innermost pixels. The small bumps seen in the line profile of Region 0 arise because the line shape varies rapidly from pixel to pixel in this region; thus, when only a limited number of pixels are averaged, the resulting spectrum is not fully smooth.

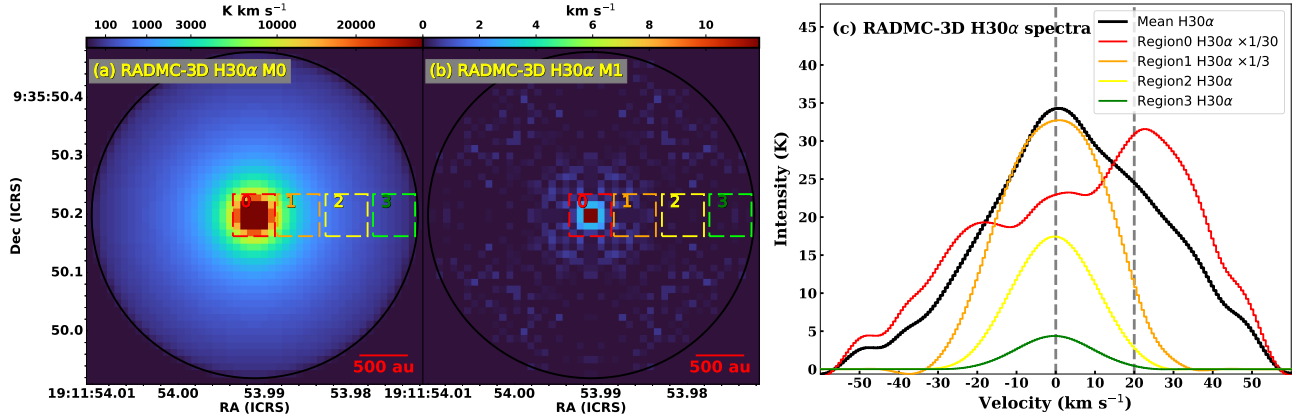


Figure 14. H30 α RADMC-3D model of an infalling HC H II region. (a and b) 0th and 1st moment maps. (c) averaged spectra over the entire region and four subregions. For clarity in the figure, the line profiles of Regions 0 and 1 have been divided by factors of 30 and 3, respectively.

REFERENCES

- Arthur, S. J., & Hoare, M. G. 2006, *ApJS*, 165, 283, doi: [10.1086/503899](https://doi.org/10.1086/503899)
- Astropy Collaboration, Price-Whelan, A. M., Lim, P. L., et al. 2022, *ApJ*, 935, 167, doi: [10.3847/1538-4357/ac7c74](https://doi.org/10.3847/1538-4357/ac7c74)
- Baudry, A., Desmurs, J. F., Wilson, T. L., & Cohen, R. J. 1997, *A&A*, 325, 255
- Beuther, H., Kuiper, R., & Tafalla, M. 2025, arXiv e-prints, arXiv:2501.16866, doi: [10.48550/arXiv.2501.16866](https://doi.org/10.48550/arXiv.2501.16866)
- Bodenheimer, P., Tenorio-Tagle, G., & Yorke, H. W. 1979, *ApJ*, 233, 85, doi: [10.1086/157368](https://doi.org/10.1086/157368)
- CASA Team, Bean, B., Bhatnagar, S., et al. 2022, *PASP*, 134, 114501, doi: [10.1088/1538-3873/ac9642](https://doi.org/10.1088/1538-3873/ac9642)
- Chomiuk, L., & Povich, M. S. 2011, *AJ*, 142, 197, doi: [10.1088/0004-6256/142/6/197](https://doi.org/10.1088/0004-6256/142/6/197)
- Churchwell, E. 2002, *ARA&A*, 40, 27, doi: [10.1146/annurev.astro.40.060401.093845](https://doi.org/10.1146/annurev.astro.40.060401.093845)
- Condon, J. J., & Ransom, S. M. 2016, *Essential Radio Astronomy* (Princeton University Press)
- De Pree, C. G., Peters, T., Mac Low, M. M., et al. 2014, *ApJL*, 781, L36, doi: [10.1088/2041-8205/781/2/L36](https://doi.org/10.1088/2041-8205/781/2/L36)
- Dullemond, C. P., Juhasz, A., Pohl, A., et al. 2012, RADMC-3D: A multi-purpose radiative transfer tool, Astrophysics Source Code Library, record ascl:1202.015
- Elitzur, M., & de Jong, T. 1978, *A&A*, 67, 323
- Fish, V. L., & Reid, M. J. 2007, *ApJ*, 670, 1159, doi: [10.1086/522329](https://doi.org/10.1086/522329)
- Fish, V. L., Reid, M. J., Argon, A. L., & Zheng, X.-W. 2005, *ApJS*, 160, 220, doi: [10.1086/431669](https://doi.org/10.1086/431669)
- Fujii, M. S., & Portegies Zwart, S. 2011, *Science*, 334, 1380, doi: [10.1126/science.1211927](https://doi.org/10.1126/science.1211927)
- Galván-Madrid, R., Rodríguez, L. F., Ho, P. T. P., & Keto, E. 2008, *ApJL*, 674, L33, doi: [10.1086/528957](https://doi.org/10.1086/528957)
- Garay, G., & Lizano, S. 1999, *PASP*, 111, 1049, doi: [10.1086/316416](https://doi.org/10.1086/316416)
- Garay, G., Rodríguez, L. F., & van Gorkom, J. H. 1986, *ApJ*, 309, 553, doi: [10.1086/164624](https://doi.org/10.1086/164624)
- Gasiprongs, N., Cohen, R. J., & Hutawarakorn, B. 2002, *MNRAS*, 336, 47, doi: [10.1046/j.1365-8711.2002.05703.x](https://doi.org/10.1046/j.1365-8711.2002.05703.x)
- Geen, S., Bieri, R., Rosdahl, J., & de Koter, A. 2021, *MNRAS*, 501, 1352, doi: [10.1093/mnras/staa3705](https://doi.org/10.1093/mnras/staa3705)
- Guzmán, A. E., Sanhueza, P., Zapata, L., Garay, G., & Rodríguez, L. F. 2020, *ApJ*, 904, 77, doi: [10.3847/1538-4357/abbe09](https://doi.org/10.3847/1538-4357/abbe09)
- Hoare, M. G. 2005, *Ap&SS*, 295, 203, doi: [10.1007/s10509-005-3690-1](https://doi.org/10.1007/s10509-005-3690-1)
- Hoare, M. G., Kurtz, S. E., Lizano, S., Keto, E., & Hofner, P. 2007, in *Protostars and Planets V*, ed. B. Reipurth, D. Jewitt, & K. Keil, 181, doi: [10.48550/arXiv.astro-ph/0603560](https://doi.org/10.48550/arXiv.astro-ph/0603560)
- Honma, M., Bushimata, T., Choi, Y. K., et al. 2005, *PASJ*, 57, 595, doi: [10.1093/pasj/57.4.595](https://doi.org/10.1093/pasj/57.4.595)
- Kalcheva, I. E., Hoare, M. G., Urquhart, J. S., et al. 2018, *A&A*, 615, A103, doi: [10.1051/0004-6361/201832734](https://doi.org/10.1051/0004-6361/201832734)

- Kavak, Ü., Sánchez-Monge, Á., López-Sepulcre, A., et al. 2021, *A&A*, 645, A29, doi: [10.1051/0004-6361/202037652](https://doi.org/10.1051/0004-6361/202037652)
- Keto, E. 2003, *ApJ*, 599, 1196, doi: [10.1086/379545](https://doi.org/10.1086/379545)
- Keto, E., Zhang, Q., & Kurtz, S. 2008, *ApJ*, 672, 423, doi: [10.1086/522570](https://doi.org/10.1086/522570)
- Keto, E. R., Welch, W. J., Reid, M. J., & Ho, P. T. P. 1995, *ApJ*, 444, 765, doi: [10.1086/175649](https://doi.org/10.1086/175649)
- Kim, K.-T., & Koo, B.-C. 2001, *ApJ*, 549, 979, doi: [10.1086/319447](https://doi.org/10.1086/319447)
- . 2003, *ApJ*, 596, 362, doi: [10.1086/377579](https://doi.org/10.1086/377579)
- Kim, W.-J., Kim, K.-T., & Kim, K.-T. 2019, *ApJS*, 244, 2, doi: [10.3847/1538-4365/ab2fc9](https://doi.org/10.3847/1538-4365/ab2fc9)
- Kim, W. J., Wyrowski, F., Urquhart, J. S., Menten, K. M., & Csengeri, T. 2017, *A&A*, 602, A37, doi: [10.1051/0004-6361/201629764](https://doi.org/10.1051/0004-6361/201629764)
- Klaassen, P. D., Johnston, K. G., Urquhart, J. S., et al. 2018, *A&A*, 611, A99, doi: [10.1051/0004-6361/201731727](https://doi.org/10.1051/0004-6361/201731727)
- Koch, E. W., & Rosolowsky, E. W. 2015, *MNRAS*, 452, 3435, doi: [10.1093/mnras/stv1521](https://doi.org/10.1093/mnras/stv1521)
- Komesh, T., Garay, G., Henkel, C., et al. 2024, *ApJ*, 967, 15, doi: [10.3847/1538-4357/ad3e7b](https://doi.org/10.3847/1538-4357/ad3e7b)
- Kudritzki, R.-P., & Puls, J. 2000, *ARA&A*, 38, 613, doi: [10.1146/annurev.astro.38.1.613](https://doi.org/10.1146/annurev.astro.38.1.613)
- Kurtz, S. 2005, in *Massive Star Birth: A Crossroads of Astrophysics*, ed. R. Cesaroni, M. Felli, E. Churchwell, & M. Walmsley, Vol. 227, 111–119, doi: [10.1017/S1743921305004424](https://doi.org/10.1017/S1743921305004424)
- Kurtz, S., Churchwell, E., & Wood, D. O. S. 1994, *ApJS*, 91, 659, doi: [10.1086/191952](https://doi.org/10.1086/191952)
- Li, S., Sanhueza, P., Zhang, Q., et al. 2023, *ApJ*, 949, 109, doi: [10.3847/1538-4357/acc58f](https://doi.org/10.3847/1538-4357/acc58f)
- Liu, H.-L., Liu, T., Evans, Neal J., I., et al. 2021, *MNRAS*, 505, 2801, doi: [10.1093/mnras/stab1352](https://doi.org/10.1093/mnras/stab1352)
- Liu, T., Evans, N. J., Kim, K.-T., et al. 2020, *MNRAS*, 496, 2790, doi: [10.1093/mnras/staa1577](https://doi.org/10.1093/mnras/staa1577)
- Liu, X., Liu, T., Zhu, L., et al. 2024, *Research in Astronomy and Astrophysics*, 24, 025009, doi: [10.1088/1674-4527/ad0d5c](https://doi.org/10.1088/1674-4527/ad0d5c)
- Men'shchikov, A. 2021, *A&A*, 649, A89, doi: [10.1051/0004-6361/202039913](https://doi.org/10.1051/0004-6361/202039913)
- Miyawaki, R., Hayashi, M., & Hasegawa, T. 2023, *PASJ*, 75, 225, doi: [10.1093/pasj/psac105](https://doi.org/10.1093/pasj/psac105)
- Möller, T., Endres, C., & Schilke, P. 2017, *A&A*, 598, A7, doi: [10.1051/0004-6361/201527203](https://doi.org/10.1051/0004-6361/201527203)
- Moscadelli, L., Cesaroni, R., Beltrán, M. T., & Rivilla, V. M. 2021, *A&A*, 650, A142, doi: [10.1051/0004-6361/202140829](https://doi.org/10.1051/0004-6361/202140829)
- Mottram, J. C., Hoare, M. G., Urquhart, J. S., et al. 2011, *A&A*, 525, A149, doi: [10.1051/0004-6361/201014479](https://doi.org/10.1051/0004-6361/201014479)
- Olguin, F. A., Sanhueza, P., Ginsburg, A., et al. 2022, *ApJ*, 929, 68, doi: [10.3847/1538-4357/ac5bd8](https://doi.org/10.3847/1538-4357/ac5bd8)
- Olguin, F. A., Sanhueza, P., Guzmán, A. E., et al. 2021, *ApJ*, 909, 199, doi: [10.3847/1538-4357/abde3f](https://doi.org/10.3847/1538-4357/abde3f)
- Olguin, F. A., Sanhueza, P., Chen, H.-R. V., et al. 2023, *ApJL*, 959, L31, doi: [10.3847/2041-8213/ad1100](https://doi.org/10.3847/2041-8213/ad1100)
- Ossenkopf, V., & Henning, T. 1994, *A&A*, 291, 943
- Peters, T., Banerjee, R., Klessen, R. S., et al. 2010a, *ApJ*, 711, 1017, doi: [10.1088/0004-637X/711/2/1017](https://doi.org/10.1088/0004-637X/711/2/1017)
- Peters, T., Longmore, S. N., & Dullemond, C. P. 2012, *MNRAS*, 425, 2352, doi: [10.1111/j.1365-2966.2012.21676.x](https://doi.org/10.1111/j.1365-2966.2012.21676.x)
- Peters, T., Mac Low, M.-M., Banerjee, R., Klessen, R. S., & Dullemond, C. P. 2010b, *ApJ*, 719, 831, doi: [10.1088/0004-637X/719/1/831](https://doi.org/10.1088/0004-637X/719/1/831)
- Qin, S.-L., Liu, T., Liu, X., et al. 2022, *MNRAS*, 511, 3463, doi: [10.1093/mnras/stac219](https://doi.org/10.1093/mnras/stac219)
- Reed, B. C. 2005, *AJ*, 130, 1652, doi: [10.1086/444474](https://doi.org/10.1086/444474)
- Rivera-Soto, R., Galván-Madrid, R., Ginsburg, A., & Kurtz, S. 2020, *ApJ*, 899, 94, doi: [10.3847/1538-4357/aba749](https://doi.org/10.3847/1538-4357/aba749)
- Robitaille, T. P., & Whitney, B. A. 2010, *ApJL*, 710, L11, doi: [10.1088/2041-8205/710/1/L11](https://doi.org/10.1088/2041-8205/710/1/L11)
- Rodríguez, L. F., Galván-Madrid, R., Sanchez-Bermudez, J., & De Pree, C. G. 2020, *ApJ*, 890, 165, doi: [10.3847/1538-4357/ab7011](https://doi.org/10.3847/1538-4357/ab7011)
- Sewilo, M., Churchwell, E., Kurtz, S., Goss, W. M., & Hofner, P. 2004, *ApJ*, 605, 285, doi: [10.1086/382268](https://doi.org/10.1086/382268)
- Suin, P., Arzoumanian, D., Zavagno, A., & Hennebelle, P. 2025, *A&A*, 698, A119, doi: [10.1051/0004-6361/202553795](https://doi.org/10.1051/0004-6361/202553795)
- Surcis, G., Vlemmings, W. H. T., van Langevelde, H. J., Hutawarakorn Kramer, B., & Bartkiewicz, A. 2019, *A&A*, 623, A130, doi: [10.1051/0004-6361/201834578](https://doi.org/10.1051/0004-6361/201834578)
- Tenorio-Tagle, G. 1979, *A&A*, 71, 59
- Tenorio-Tagle, G., Yorke, H. W., & Bodenheimer, P. 1979, *A&A*, 145, 110
- Urquhart, J. S., Wells, M. R. A., Pillai, T., et al. 2022, *MNRAS*, 510, 3389, doi: [10.1093/mnras/stab3511](https://doi.org/10.1093/mnras/stab3511)
- Vacca, W. D., Garmany, C. D., & Shull, J. M. 1996, *ApJ*, 460, 914, doi: [10.1086/177020](https://doi.org/10.1086/177020)
- van Buren, D., & Mac Low, M.-M. 1992, *ApJ*, 394, 534, doi: [10.1086/171604](https://doi.org/10.1086/171604)
- van Buren, D., Mac Low, M.-M., Wood, D. O. S., & Churchwell, E. 1990, *ApJ*, 353, 570, doi: [10.1086/168645](https://doi.org/10.1086/168645)
- Vink, J. S., de Koter, A., & Lamers, H. J. G. L. M. 2001, *A&A*, 369, 574, doi: [10.1051/0004-6361:20010127](https://doi.org/10.1051/0004-6361:20010127)
- Wilkin, F. P. 1996, *ApJL*, 459, L31, doi: [10.1086/309939](https://doi.org/10.1086/309939)

- Wilson, T. L., Rohlfs, K., & Hüttemeister, S. 2013, *Tools of Radio Astronomy* (Springer),
doi: [10.1007/978-3-642-39950-3](https://doi.org/10.1007/978-3-642-39950-3)
- Winnberg, A., Nguyen-Quang-Rieu, Johansson, L. E. B., & Goss, W. M. 1975, *A&A*, 38, 145
- Wood, D. O. S., & Churchwell, E. 1989, *ApJS*, 69, 831,
doi: [10.1086/191329](https://doi.org/10.1086/191329)
- Wu, Y. W., Reid, M. J., Sakai, N., et al. 2019, *ApJ*, 874, 94, doi: [10.3847/1538-4357/ab001a](https://doi.org/10.3847/1538-4357/ab001a)
- Xu, F., Wang, K., Liu, T., et al. 2024, *Research in Astronomy and Astrophysics*, 24, 065011,
doi: [10.1088/1674-4527/ad3dc3](https://doi.org/10.1088/1674-4527/ad3dc3)
- Yang, A. Y., Thompson, M. A., Tian, W. W., et al. 2019, *MNRAS*, 482, 2681, doi: [10.1093/mnras/sty2811](https://doi.org/10.1093/mnras/sty2811)
- Yang, A. Y., Urquhart, J. S., Thompson, M. A., et al. 2021, *A&A*, 645, A110, doi: [10.1051/0004-6361/202038608](https://doi.org/10.1051/0004-6361/202038608)
- Yang, A. Y., Thompson, M. A., Urquhart, J. S., et al. 2025a, *A&A*, 694, A26,
doi: [10.1051/0004-6361/202452078](https://doi.org/10.1051/0004-6361/202452078)
- Yang, D., Liu, H.-L., Liu, T., et al. 2025b, arXiv e-prints, arXiv:2508.03229, doi: [10.48550/arXiv.2508.03229](https://doi.org/10.48550/arXiv.2508.03229)
- Zapata, L. A., Fernández-López, M., Leurini, S., et al. 2023, *ApJL*, 956, L35, doi: [10.3847/2041-8213/acfe71](https://doi.org/10.3847/2041-8213/acfe71)
- Zhang, C., Zhu, F.-Y., Liu, T., et al. 2023, *MNRAS*, 520, 3245, doi: [10.1093/mnras/stad190](https://doi.org/10.1093/mnras/stad190)
- Zhang, S., Liu, T., Wang, K., et al. 2024, *MNRAS*, 535, 1364, doi: [10.1093/mnras/stae2415](https://doi.org/10.1093/mnras/stae2415)
- Zhu, F.-Y., Zhu, Q.-F., Li, J., Zhang, J.-S., & Wang, J.-Z. 2015, *ApJ*, 812, 87, doi: [10.1088/0004-637X/812/1/87](https://doi.org/10.1088/0004-637X/812/1/87)
- Zhu, Q.-F., Lacy, J. H., Jaffe, D. T., Richter, M. J., & Greathouse, T. K. 2008, *ApJS*, 177, 584,
doi: [10.1086/588731](https://doi.org/10.1086/588731)